COSMIC EVOLUTION OF THE CORRELATION BETWEEN SUPERMASSIVE BLACK HOLE MASS AND HOST GALAXY AT REDSHIFT UP TO 1.7

Xuheng Ding[1, 2], John Silverman[3], Tommaso Treu[2], Federica Duras[4, 5], Angela Bongiorno[5], Andreas Schulze[6], Malte Schramm[6], Simon Birrer[2], Knud Jahnke, et al.

Draft version January 29, 2019

ABSTRACT

We investigate the cosmic evolution of the relation supermassive black hole and host galaxy properties at $1.2 < z < 1.7$, using a sample of 32 X-ray selected type-1 AGN obtained with the Hubble Space Telescope (*HST*). The high-resolution *HST* images enable us to decompose the AGN image and infer the host properties including luminosities ($L_{\rm host}$) and stellar masses (M_*). We estimate the BH masses ($\mathcal{M}_{\rm BH}$) with spectroscopic information of the $H\alpha$, $H\beta$. We compare the $\mathcal{M}_{\rm BH}$-$L_{\rm host}$ and $\mathcal{M}_{\rm BH}$-M_* relation to the local active galaxies and taking the selection effects into account. Results to be written. To be written.

Subject headings: galaxies: active — galaxies: evolution

1. INTRODUCTION

Most galactic nuclei are thought to harbor a supermassive black hole (BH), whose mass ($\mathcal{M}_{\rm BH}$) is well known to be correlated with the host properties, such as $\mathcal{M}_{\rm BH}$-host luminosity ($L_{\rm host}$), $\mathcal{M}_{\rm BH}$-stellar mass (M_*) and $\mathcal{M}_{\rm BH}$-stellar velocity dispersion(σ_*). These tight correlations indicate a connection between nuclear activity and galaxy formation and evolution (e.g., Magorrian et al. 1998; Ferrarese & Merritt 2000; Marconi & Hunt 2003; Gültekin et al. 2009; Beifiori et al. 2012; Häring & Rix 2004; Gebhardt et al. 2001; Graham et al. 2011). Currently, the physical mechanism that can produce such a tight relationship is unknown, due to the daunting range of scales between the BHs dynamical sphere and their host galaxy. On the one hand, cosmological simulations of structure formation are able to reproduce the mean local correlations considering the active galactic nucleus (AGN) feedback as the physical driver (Springel et al. 2005; Hopkins et al. 2008; Di Matteo et al. 2008; DeGraf et al. 2015). On the other hand, Peng (2007); Jahnke & Macciò (2011); Hirschmann et al. (2010) show that, without the need of physical coupling, another possibility is a statistical convergence from the galaxy mergers which reproduces the observed correlations.

A powerful way to understand the origin of these correlations is to study them as a function of redshift, determining how and when they emerged and evolved over cosmic time (e.g., Treu et al. 2004; Salviander et al. 2006; Woo et al. 2006; Jahnke et al. 2009; Schramm & Silverman 2013). Dur-

dxh@astro.ucla.edu
[1] School of Physics and Technology, Wuhan University, Wuhan 430072, China
[2] Department of Physics and Astronomy, University of California, Los Angeles, CA, 90095-1547, USA
[3] Kavli IPMU (WPI), UTIAS, The University of Tokyo, Kashiwa, Chiba 277-8583, Japan
[4] Dipartimento di Matematica e Fisica, Universit Roma Tre, via della Vasca Navale 84, I-00146, Roma, Italy
[5] INAF Osservatorio Astronomico di Roma, via Frascati 33, 00040 Monteporzio Catone, Italy
[6] National Astronomical Observatory of Japan, Mitaka, Tokyo 181-8588, Japan

ing the past decade, there has been much progress on this front at $z < 1$ using type 1 AGNs. For example, the work by Park et al. (2015); Treu et al. (2007); Peng et al. (2006) demonstrated that $\mathcal{M}_{\rm BH}$ at fixed bulge luminosity compared to the local relations. This offset is consistent with a scenario in which supermassive BHs were built up first with galaxy then growing around their deep potential wells. Similarly, the works by Bennert et al. (2011); Woo et al. (2008) agreed to this scenario by studying the $\mathcal{M}_{\rm BH}$-M_* and $\mathcal{M}_{\rm BH}$-σ_* relations. Nevertheless, the evolution is detected at low significance given the considerable error bars, and some studies report results consistent with no evolution Schramm & Silverman (2013); Sun et al. (2015); Cisternas et al. (2011).

In order to make progress it is important to reduced as much as possible the uncertainties and take great care of selection effects and systematic errors. First, one needs to deal with the inherent uncertainties in BH mass estimates using the so-called "virial" method. In particular, many studies rely on $\mathcal{M}_{\rm BH}$ estimates using the $C_{\rm IV}$ (or $Mg_{\rm II}$) line that may have unknown systematics, such as non-virial component of the BLR gas, when compared to local samples with masses based on broad Balmer lines (i.e. $H\alpha$ and $H\beta$, Schulze et al. 2018; Baskin & Laor 2005; Trakhtenbrot & Netzer 2012). Second, since the host information is swamped by the bright nuclear light, measuring the host galaxy properties is challenging. Great care is required for modeling the point spread function and whenever possible it is beneficial to study lensed quasars, since lensing magnifies the host image to lensed arcs (Peng et al. 2006; Ding et al. 2017a,b). Last but not least, the selection function needs to be taken into account when intepreting the observations (**??**). For instance, it has been demonstrated (Schulze & Wisotzki 2011, 2014) that selecting bright AGNs at high redshift results in display steeper slopes than random ones, suggesting the selecting effects can exhibit faster evolution than a random sample. It is also important to consider the selection function when comparing the observed scaling relations with simulated ones (DeGraf et al. 2015).

In this study, we aim to make progress by making use of a large sample with high-quality data both for the measure-

ment of both the host properties and the $\mathcal{M}_{\mathrm{BH}}$, extending to the highest redshifts where evolutionary effects should be strongest (DeGraf et al. 2015). In practice, we aim to determine whether AGNs have begun to couple to their host galaxy at $1.2 < z < 1.7$, an epoch when supermassive BH close to its peak accretion history (Aird et al. 2015). In this redshift range, we measure 32 host galaxies properties using *HST* imaging data, and estimate their $\mathcal{M}_{\mathrm{BH}}$ based on the robust $H\alpha$ and $H\beta$, using the multi-object spectrograph Subaru/FMOS. Our study overcomes the biases in the following way. First, to minimize selection bias, we select AGNs that fall below the knee of the black hole mass function. Second, we estimate $\mathcal{M}_{\mathrm{BH}}$ using Balmer lines which avoids the systematics by Mg$_{\mathrm{II}}$. Third, our X-ray selected sample have lower nuclear-to-host ratios which facilitate the galaxy mass measurements. Moreover, 21/32 systems in our sample have two-band *HST* data (i.e. WFC3+ACS), whose multi-band information provides reliable K-correction and stellar mass inference. Given the high-quality data at such redshift, we can test whether the growth of BH predates that of the host by a factor of at least 1.7 (~ 0.23 dex).

The paper is organized as follows. We briefly describe the sample selection, observation and data reduction in Section 2. We infer the host galaxy surface photometry and $\mathcal{M}_{\mathrm{BH}}$ in Section 3. In Section 4, we present our main result by adopting K-correction and SED fitting, to infer the rest-frame R band L_{host} and M_* in order to compare with the local samples. Discussion and conclusion are presented in Section 5 and Section 6.

Throughout this paper, we adopt a standard concordance cosmology with $H_0 = 70$ km s^{-1} Mpc^{-1}, $\Omega_m = 0.30$, and $\Omega_\Lambda = 0.70$. Magnitudes are given in the AB system.

2. OBSERVATIONS AND DATA REDUCTION

In this section, we summarize the sample selection, observations, and data reduction of our sample.

2.1. *Sample selection*

We aim to study the relation between the BH masses ($\mathcal{M}_{\mathrm{BH}}$) and their host galaxy properties including luminosities (L_{host}) and stellar mass (M_*) to redshift at $z > 1$. For this propose, we focus on the broad-line (type-1) AGNs as provided by the X-ray coverage of COSMOS (Civano et al. 2016), (E)-CDFS-S (Lehmer et al. 2005; Xue et al. 2011), and SXDS (Ueda et al. 2008) fields. We select the broad-line AGNs at redshift region $1.2 < z < 1.7$ which cover a BH range $7.5 < \log\mathcal{M}_{\mathrm{BH}} < 8.5$. The Near IR spectra of AGNs are available from the survey of Subaru's Fiber Multi-Object Spectrograph (FMOS, Kimura et al. 2010; Schulze et al. 2018), a near-infrared (0.9-1.8 μm) spectrograph have with 400 apertures. The FMOS survey provides the best $\mathcal{M}_{\mathrm{BH}}$ estimates by $H\alpha$ and $H\beta$ lines out to $z \sim 1.7$ (Greene & Ho 2005; Matsuoka et al. 2013; Nobuta et al. 2012). Overall, our final sample is composed of 32 new observations by HST/WFC3. Table 1 list all the AGN systems analyzed in this work.

For the calibration with the local relation, we use 19 local AGN measurements (Bennert et al. 2010; Peterson et al. 2004) which define the zero-point. To compare with the samples in the literature, we also adopt the samples from Ding et al. (2017b), which include the measurements by Peng et al. (2006); Park et al. (2015) to study the $\mathcal{M}_{\mathrm{BH}}$-$L_{\mathrm{host}}$ of 127 objects by *HST*.

2.2. *Observation and reduction*

2.2.1. *HST image Observation*

The high spatial resolution of the host image is required for the decomposition of the nuclear/host emission and the accurate estimate of the host stellar mass. All the new 32 AGN systems were observed with the HST/WFC3 infrared channel, as the HST program GO-15115, PI: John Silverman. We selected to use the filters F125W ($1.2 < z < 1.44$) and F140W ($1.44 < z < 1.7$) according to the redshift of the targets. This selection ensures that the broad $H\alpha$ line ($4000\mathring{A}$) is not present in the bandpass so as not to contaminate the host emissions due to the broad wings of the PSF.

For each of the 32 new AGNs we took six separate exposures with $\sim 399s$ (i.e. total exposure time $\sim 2394s$). The six exposures for each dither image were combined with the ASTRODRIZZLE software package, with an output pixel scale of $0\rlap{.}''0642$ by setting `pixfrac` parameter as 0.8 using the `gaussian` kernel. To accurately estimate the background light which could come from both the sky and the detector, we adopt the PHOTUTILS to measure the photometry.

Multi-band information provides the spectral energy distributions (SED) at a more precise level. 21/32 of our sample have rest-frame UV images by Scoville et al. (2007). Images were taken through the wide ACS/F814W filter at four dither pointing with $507s$ exposures. The final image is drizzled to $0\rlap{.}''03$ pixel scale. Given the multi-band image for these systems, we are able to infer their host color and assess the contribution of both the young and old stellar population to the stellar mass budge Gallazzi & Bell (2009) which insures an accurate inference of rest-frame R-band luminosity by K-correction, stellar mass and star formation rate (SFR).

2.2.2. *AGN Emission Line*

The $\mathcal{M}_{\mathrm{BH}}$ of type-1 AGNs can be inferred using the so-called virial method (Peterson et al. 2004; Shen 2013). The kinematics of the broad-line region (BLR) trace the gravitational field of the central supermassive black hole, assuming the gravity dominates the motion of the BLR gas. In this scenario, the width of the emission-line provided the scale of the velocity, while the AGN continuum luminosity establish an empirical scale of the BLR size. As a result, the estimation of the $\mathcal{M}_{\mathrm{BH}}$ is achieved by these measurements.

For our targets, the $H\alpha$ and $H\beta$ emission-line properties have been investigated by Schulze et al. (2018) using the multi-object spectrograph Subaru/FMOS. We referred to that paper for the details of continuum fitting and emission line modeling. Since the other compared AGNs in the literature used different calibrations of the virial method, we compare the difference among the recipes by Schulze et al. (2018); McGill et al. (2008); Ding et al. (2017b) and adopt a list of consistent ones to cross-calibrate the $\mathcal{M}_{\mathrm{BH}}$ for all the samples, in order to avoid any systematic bias in Section 3.2.

3. ANALYSIS

3.1. *Surface Photometry*

3.1.1. *PSF library*

The knowledge of the PSF is crucial for the AGN imaging decomposition, especially when the nuclear image is unresolved with light distributed as the point source. The PSF is known to be vary across the detector and with time, due to the effect of aberrations and breathing. Simulated PSF, such

as TINYTIM ones, are usually insufficient matches to observations for our purposes Mechtley et al. (2012). Stars within the fields provide a better description than the simulated PSF, since they were observed simultaneously with the science targets and reduced and analyzed in the same way Kim et al. (2008); Park et al. (2015)

To minimize the impact of the mismatch, we build a PSF library by selecting all the isolated, unsaturated PSF-stars with high S/N from our entire program. The selection consists of the following steps. We first adopt the identified stars as candidates from the COSMOS2015 catalog by Laigle et al. (2016). A lot of bright stars with intensity similar to the AGNs were excluded by Laigle et al. (2016); in the second step, we manually select the PSF-like objects as candidates. We then remove the non-ideal PSF candidates based on their intensity, FWHM, central symmetry and any that were contaminated by nearby objects. In the end, the PSF library contains 78 and 36 PSFs for F140W and F125W, respectively.

We assume that the stars in the library are representative of the possible PSFs in our program. Therefore, we assume that the PSF library gives a good representation of the dominant source of uncertainty as well as the best fit.

3.1.2. *AGN-host Decomposition*

We simultaneously fit the two-dimensional flux distribution of the center nuclear and the underlying host galaxy. Following common practice, we assume the unresolved nuclear as a scaled point source, while the host galaxy as a Sérsic profile. Note that the actual morphologies of the host galaxies could be more complicated (e.g. bulge+disk). However, the purpose of adopting the Sérsic model is a simplified a first-order approximation of the surface brightness distribution with a flexible parameterization which provides sufficient freedom to infer the host flux, given the high redshift range of our sample. Furthermore, we fit other galaxies that happen to be close to the AGN as additional Sérsic model, to account for any potential contamination.

We adopt the imaging modeling tool LENSTRONOMY (Birrer & Amara 2018) to perform the decomposition of the host and nuclear light. LENSTRONOMY is a multi-purpose open-source gravitational lens image modeling python package. Its flexibility enables us to turn off the lensing channel and focus on the AGN decomposition[7]. The maim advantage over GALFIT is that LENSTRONOMYreturns the full posterior of the parameter and not just the best fit model and the Laplace approximation of the uncertainties. The input ingredients to LENSTRONOMY include:

1. AGN imaging data.
   – Using aperture photometry, we find that an aperture size with radius $\sim 1''5$ covers sufficient AGN light our samples. By default, we cut out the AGN image to a 61×61 pixels box (i.e. $4'' \times 4''$). If needed, the larger size box would be sufficient to include the nearby objects.

2. Noise level map.
   – The origin of the noise in each pixel stems from the read noise, background noise and Poisson noise by the astronomical sources themselves. To take them into

account, we measure the read noise and background noise level directly from the empty regions of the data. We calculate the effective exposure time of each pixel based on the drizzled WHT array maps to infer the Poisson noise level.

3. PSF.
   – The PSF is directly taken from the PSF library. Usually, a mismatch exists when subtracting the AGN as the scaled PSF, especially at the central parts. While modeling multiply imaged AGN, this mismatch can be mitigated with PSF reconstruction by the iterative method (Chen et al. 2016; Birrer et al. 2018). However, this approach requires multiple images which are not available in our case. We remedy this deficiency by using a broad library which should contain sufficient information to cover all the possible PSF.

The host properties of one AGN system is inferred via the following steps. First, we model the AGN and host using each PSFs in the library. Inputting the fitting ingredients to LENSTRONOMY, the posterior distribution of the parameter space is calculated and optimized by adopting the Particle Swarm Optimizer (PSO)[8]. To avoid any unphysical inferences, we set the upper and lower limit for the key parameters as effective radius $R_{\mathrm{eff}} \in [0''1, 1'']$, and Sersic index $n \in [1, 7]$. Then, we rank the performance of each PSF based on the χ^2 value and select the top-eight PSFs as representative of the best fit PSFs. We infer the host property (i.e., host flux, R_{eff}, Sersic index n) using a weighted arithmetic mean. The weight is calculated by:

$$w_i = exp\left(-\alpha \frac{(\chi_i^2 - \chi_{best}^2)}{2\chi_{best}^2}\right), \tag{1}$$

where the α is an inflation parameter so that when $i = 8$:

$$\alpha \frac{\chi_{i=8}^2 - \chi_{best}^2}{2\chi_{best}^2} = 2, \tag{2}$$

The goal of this recipe is to weight each PSF based on their relative goodness of fit, while ensuring at least eight are used to capture the range of systematic uncertainties. The answers would not change significantly if we had chosen a different number of PSFs, as we show below.

Note that since each AGN system was observed in different location of the detector and at a different time, the top-eight PSFs usually vary from one AGN system to another. Given the weights, the inferred value of host properties and the root-mean-square (σ) are calculated as:

$$\bar{x} = \frac{\sum_{i=1}^{8} x_i * w_i}{\Sigma w_i}, \tag{3}$$

$$\sigma = \sqrt{\frac{\sum_{i=1}^{8} (x_i - \bar{x})^2 * w_i}{\Sigma w_i}}. \tag{4}$$

In Figure 1, we demonstrate the optimized results inferred by LENSTRONOMY, including the AGN images, best-fit models, image subtract point source (i.e. host) and the residuals.

---

[7] For a sanity check, we compared the performance of LENSTRONOMY to the most commonly used galaxy modeling software GALFIT and confirm that the consistent result could be obtained with the same fitting ingredients provided.

[8] Note that, the LENSTRONOMY enables one to further infer the parametric confidence interval using MCMC. However, in our case, given a fixed PSF, the $1 - \sigma$ inference of each parameter are extremely narrow.

As an example, the weights adopted in the analysis of system COSMOS-CID1174 are listed in Table 2. In order to quickly overview our inference, we summarize the relations of the properties between effective radius $R_{\rm eff}$, 2) Sérsic index n and 3) host to total flux ratio in Figure 2.

The inference of the host properties is weighted by eight top-ranked PSFs. To understand how the choice of the number of top-ranked PSF affects our inference, we compare to the one inferred by five and ten top-ranked PSFs. As shown in Figure 3, the results are very consistent, meaning that the host inference is solid when the amount of selected PSF exceeds five. For a smaller number of PSFs one tends to underestimate the uncertainties.

18/32 systems in the COSMOS field have ACS/F184W imaging data. We infer their host properties using the same approach used for the WFC3-IR data. The field of view by ACS are larger than WFC3, and we collected in total 174 ACS PSFs in the library. In principle, the host inference by IR band is superior to the one by UV band, giving that the effects of dust extinction and contrast between the (blue) AGN and (red) host. Thus, we fix the $R_{\rm eff}$ and Sérsic n as the value inferred by IR band, assuming that the morphology of the galaxy is consistent between ACS and WFC3.

We list all the inference of the host galaxy properties in the Table 3.

3.1.3. *Host luminosity and stellar mass*

To be written:

1. Describe the SED fitting and the ground-based photometry data.

2. The comparison of our host-to-total flux ratios to the SED decomposed ones.

3. The inferred rest-frame R band magnitude and stellar mass.

Having inferred the value of the rest-frame R-band magnitude, the luminosity is derived by $\log L_R/L_{R,\odot} = 0.4(M_{R,\odot} - M_R)$, where $M_{R,\odot} = 4.61$ (Blanton & Roweis 2007).

Introduce the passive evolution?

To directly compare with local samples, we consider the passive evolution scenario for the inferred $L_{\rm host}$ and transfer to its expected value at today.

We summarized the inferred R-band luminosities in Table 3.

3.2. *BH masses*

To avoid any systematic bias between our samples and the literature ones, we compared the recipes as introduced by Schulze et al. (2018); Ding et al. (2017b). We find that the $H\beta$ estimator is very consistent (< 0.03 dex) between the two references. Moreover, in Schulze et al. (2018), the cross-calibrate between the $H\alpha$ and $H\beta$ are consistent. Thus, we adopt the virial formalism from Schulze et al. (2018):

$$\log\left(\frac{\mathcal{M}_{\rm BH}(H\beta)}{M_\odot}\right) = 6.91 + 0.50\log\left(\frac{\lambda L_{\lambda_{5100}}}{10^{44}{\rm erg\ s}^{-1}}\right)$$
$$+ 2.0\log\left(\frac{{\rm FWHM}(5100)}{1000\ {\rm km\ s}^{-1}}\right), \quad (5)$$

and

$$\log\left(\frac{\mathcal{M}_{\rm BH}(H\alpha)}{M_\odot}\right) = 6.71 + 0.48\log\left(\frac{\lambda L_{H\alpha}}{10^{42}{\rm erg\ s}^{-1}}\right)$$
$$+ 2.12\log\left(\frac{{\rm FWHM}(H\alpha)}{1000\ {\rm km\ s}^{-1}}\right). \quad (6)$$

Having defined the recipes, we estimate the $\mathcal{M}_{\rm BH}$ by adopting the emission line properties measured by Schulze et al. (2018). 14 of the overall systems have both $H\alpha$ and $H\beta$ emission line information; we adopt the averaged $\mathcal{M}_{\rm BH}$ value. We summarized the inference of the $\mathcal{M}_{\rm BH}$ together with the properties of the emission line in Table 4.

4. RESULTS

4.1. $\mathcal{M}_{\rm BH}$-$L_{\rm host}$ *relation*

4.2. $\mathcal{M}_{\rm BH}$-M_* *relation*

4.2.1. *Stellar mass estimates*

stellar mass

5. SUMMARY

6. DISCUSS

6.1. *Systematic error*

6.2. *Masks objects for the COSMOS-CID206 and ECDFS-358*

ACKNOWLEDGMENTS

We thank the people who discuss with the paper.

REFERENCES

Aird, J., Coil, A. L., Georgakakis, A., et al. 2015, MNRAS, 451, 1892 1
Baskin, A., & Laor, A. 2005, MNRAS, 356, 1029 1
Beifiori, A., Courteau, S., Corsini, E. M., & Zhu, Y. 2012, MNRAS, 419, 2497 1
Bennert, V. N., Auger, M. W., Treu, T., Woo, J.-H., & Malkan, M. A. 2011, ApJ, 742, 107 1
Bennert, V. N., Treu, T., Woo, J., et al. 2010, ApJ, 708, 1507 2.1
Birrer, S., & Amara, A. 2018, Physics of the Dark Universe, 22, 189 3.1.2
Birrer, S., Treu, T., Rusu, C. E., et al. 2018, arXiv e-prints, arXiv:1809.01274 3
Blanton, M. R., & Roweis, S. 2007, AJ, 133, 734 3.1.3
Chen, G. C.-F., Suyu, S. H., Wong, K. C., et al. 2016, MNRAS, 462, 3457 3
Cisternas, M., Jahnke, K., Bongiorno, A., et al. 2011, ApJ, 741, L11 1
Civano, F., Marchesi, S., Comastri, A., et al. 2016, ApJ, 819, 62 2.1
DeGraf, C., Di Matteo, T., Treu, T., et al. 2015, MNRAS, 454, 913 1
Di Matteo, T., Colberg, J., Springel, V., Hernquist, L., & Sijacki, D. 2008, ApJ, 676, 33 1
Ding, X., Liao, K., Treu, T., et al. 2017a, MNRAS, 465, 4634 1
Ding, X., Treu, T., Suyu, S. H., et al. 2017b, MNRAS, 472, 90 1, 2.1, 2.2.2, 3.2
Ferrarese, L., & Merritt, D. 2000, ApJ, 539, L9 1

Gallazzi, A., & Bell, E. F. 2009, ApJS, 185, 253 2.2.1
Gebhardt, K., Bender, R., Bower, G., et al. 2001, ApJ, 555, L75 1
Graham, A. W., Onken, C. A., Athanassoula, E., & Combes, F. 2011, MNRAS, 412, 2211 1
Greene, J. E., & Ho, L. C. 2005, ApJ, 630, 122 2.1
Gültekin, K., Richstone, D. O., Gebhardt, K., et al. 2009, ApJ, 698, 198 1
Häring, N., & Rix, H.-W. 2004, ApJ, 604, L89 1
Hirschmann, M., Khochfar, S., Burkert, A., et al. 2010, MNRAS, 407, 1016 1
Hopkins, P. F., Hernquist, L., Cox, T. J., & Kereš, D. 2008, ApJS, 175, 356 1
Jahnke, K., & Macciò, A. V. 2011, ApJ, 734, 92 1
Jahnke, K., Bongiorno, A., Brusa, M., et al. 2009, ApJ, 706, L215 1
Kim, M., Ho, L. C., Peng, C. Y., Barth, A. J., & Im, M. 2008, ApJS, 179, 283 3.1.1
Kimura, M., Maihara, T., Iwamuro, F., et al. 2010, PASJ, 62, 1135 2.1
Laigle, C., McCracken, H. J., Ilbert, O., et al. 2016, ApJS, 224, 24 3.1.1
Lehmer, B. D., Brandt, W. N., Alexander, D. M., et al. 2005, ApJS, 161, 21 2.1
Magorrian, J., Tremaine, S., Richstone, D., et al. 1998, AJ, 115, 2285 1
Marconi, A., & Hunt, L. K. 2003, ApJ, 589, L21 1
Matsuoka, K., Silverman, J. D., Schramm, M., et al. 2013, ApJ, 771, 64 2.1

TABLE 1
SAMPLE PROPERTIES.

Object ID	z	WFC3/Filter	RA	DEC
(1)	(2)	(3)	(4)	(5)
COSMOS-CID1174	1.552	F140W	150.2789	1.9595
COSMOS-CID1281	1.445	F140W	150.4160	2.5258
COSMOS-CID206	1.483	F140W	149.8371	2.0088
COSMOS-CID216	1.567	F140W	149.7918	1.8729
COSMOS-CID237	1.618	F140W	149.9916	1.7243
COSMOS-CID255	1.664	F140W	150.1017	1.8483
COSMOS-CID3242	1.532	F140W	149.7113	2.1452
COSMOS-CID3570	1.244	F125W	149.6411	2.1076
COSMOS-CID452	1.407	F125W	150.0045	2.2371
COSMOS-CID454	1.478	F140W	149.8681	2.3307
COSMOS-CID50	1.239	F125W	150.2080	2.0833
COSMOS-CID543	1.301	F125W	150.4519	2.1448
COSMOS-CID597	1.272	F125W	150.5262	2.2449
COSMOS-CID607	1.294	F125W	150.6097	2.3231
COSMOS-CID70	1.667	F140W	150.4051	2.2701
COSMOS-LID1273	1.617	F140W	150.0565	1.6275
COSMOS-LID1538	1.527	F140W	150.6215	2.1588
COSMOS-LID360	1.579	F140W	150.1251	2.8617
COSMOS-XID2138	1.551	F140W	149.7036	2.5781
COSMOS-XID2202	1.516	F140W	150.6530	1.9969
COSMOS-XID2396	1.600	F140W	149.4779	2.6425
CDFS-1	1.630	F140W	52.8990	-27.8600
CDFS-229	1.326	F125W	53.0680	-27.6580
CDFS-321	1.570	F140W	53.0486	-27.6239
CDFS-724	1.337	F125W	53.2870	-27.6940
ECDFS-358	1.626	F140W	53.0850	-28.0370
SXDS-X1136	1.325	F125W	34.8925	-5.1498
SXDS-X50	1.411	F125W	34.0267	-5.0602
SXDS-X717	1.276	F125W	34.5400	-5.0334
SXDS-X735	1.447	F140W	34.5581	-4.8781
SXDS-X763	1.412	F125W	34.5849	-4.7864
SXDS-X969	1.585	F140W	34.7594	-5.4291

NOTE. — Column 1: Object field and ID. Column 2: Redshifts. Column 3: WFC3 filter. Note that the targets from the COSMOS field also have ACS/F814W imaging. Column 4 and 5: J2000 RA and DEC coordinates.

McGill, K. L., Woo, J., Treu, T., & Malkan, M. A. 2008, ApJ, 673, 703 2.2.2

Mechtley, M., Windhorst, R. A., Ryan, R. E., et al. 2012, ApJ, 756, L38 3.1.1

Nobuta, K., Akiyama, M., Ueda, Y., et al. 2012, ApJ, 761, 143 2.1

Park, D., Woo, J.-H., Bennert, V. N., et al. 2015, ApJ, 799, 164 1, 2.1, 3.1.1

Peng, C. Y. 2007, ApJ, 671, 1098 1

Peng, C. Y., Impey, C. D., Rix, H.-W., et al. 2006, ApJ, 649, 616 1, 2.1

Peterson, B. M., Ferrarese, L., Gilbert, K. M., et al. 2004, ApJ, 613, 682 2.1, 2.2.2

Salviander, S., Shields, G. A., Gebhardt, K., & Bonning, E. W. 2006, New Astronomy Review, 50, 803 1

Schramm, M., & Silverman, J. D. 2013, ApJ, 767, 13 1

Schulze, A., & Wisotzki, L. 2011, A&A, 535, A87 1

—. 2014, MNRAS, 438, 3422 1

Schulze, A., Silverman, J. D., Kashino, D., et al. 2018, ArXiv e-prints, arXiv:1810.07445 1, 2.1, 2.2.2, 3.2, 3.2

Scoville, N., Abraham, R. G., Aussel, H., et al. 2007, ApJS, 172, 38 2.2.1

Shen, Y. 2013, Bulletin of the Astronomical Society of India, 41, 61 2.2.2

Springel, V., White, S. D. M., Jenkins, A., et al. 2005, Nature, 435, 629 1

Sun, M., Trump, J. R., Brandt, W. N., et al. 2015, ApJ, 802, 14 1

Trakhtenbrot, B., & Netzer, H. 2012, MNRAS, 427, 3081 1

Treu, T., Malkan, M. A., & Blandford, R. D. 2004, ApJ, 615, L97 1

Treu, T., Woo, J.-H., Malkan, M. A., & Blandford, R. D. 2007, ApJ, 667, 117 1

Ueda, Y., Watson, M. G., Stewart, I. M., et al. 2008, ApJS, 179, 124 2.1

Woo, J., Treu, T., Malkan, M. A., & Blandford, R. D. 2006, ApJ, 645, 900 1

Woo, J.-H., Treu, T., Malkan, M. A., & Blandford, R. D. 2008, ApJ, 681, 925 1

Xue, Y. Q., Luo, B., Brandt, W. N., et al. 2011, ApJS, 195, 10 2.1

TABLE 2
DETAILS OF CID1174'S INFERENCE.

PSF rank (1)	total χ^2 (2)	weights w_i (3)	host flux (counts) (4)	host flux ratio (5)	R_{eff}(arcsec) (6)	Sérsic n (7)
1	8584.429	1.000	82.209	35.4%	0.″345	1.114
2	8646.711	0.920	99.102	41.9%	0.″298	1.932
3	8816.947	0.734	76.74	33.0%	0.″365	1.102
4	9304.841	0.383	128.618	54.7%	0.″231	2.78
5	9652.575	0.241	187.498	79.0%	0.″116	6.175
6	9917.101	0.170	100.166	42.3%	0.″287	2.066
7	10018.324	0.148	75.061	32.3%	0.″365	1.226
8	10087.456	0.135	79.835	34.3%	0.″358	1.195
Weighted value			97.322 ± 28.336	$41.5\% \pm 11.7\%$	$0.″309 \pm 0.″065$	1.862 ± 1.26

NOTE. — Column 1: Rank of the PSF from the library. Column 2: Total χ^2 for the corresponding PSF. Column 3: Weights for the inference. Column 4-7: Fitted value for the host flux, host/total flux ratio, effective radius, and Sérsic index. For this sample, the inflation parameter α calculated by Eq. 2 is 16.671.

TABLE 3
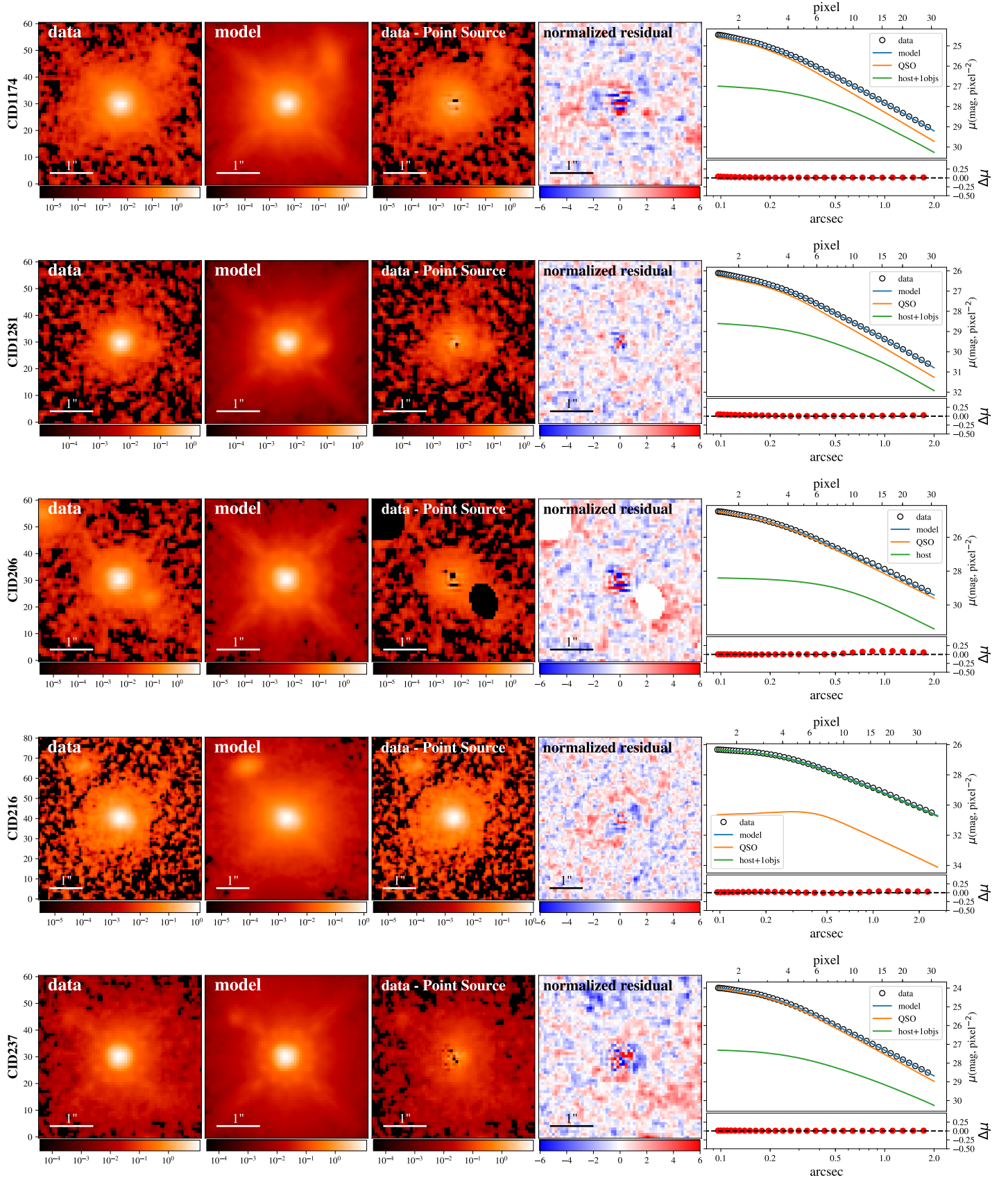INFERRED HOST GALAXY PARAMETERS FOR THE 32 SYSTEMS.

Target ID (1)	WFC3					ACS			$\log L_R$ $(L_{\odot,R})$ (10)
	reduced χ^2 (2)	host-to-total flux ratio (3)	R_{eff} (″) (4)	Sérsic n (5)	magnitude (AB system) (6)	reduced χ^2 (7)	host-to-total flux ratio (8)	magnitude (AB system) (9)	
CID1174	2.307	$41.5\% \pm 11.7\%$	$0.″309 \pm 0.″065$	1.862 ± 1.26	$21.482^{+0.374}_{-0.277}$	2.496	$11.2\% \pm 1.1\%$	$23.214^{+0.113}_{-0.103}$	
CID1281	1.322	$49.3\% \pm 13.7\%$	$0.″239 \pm 0.″094$	3.146 ± 1.483	$22.879^{+0.362}_{-0.271}$	1.378	$18.5\% \pm 7.7\%$	$24.828^{+0.595}_{-0.382}$	
CID206	2.054	$35.3\% \pm 24.3\%$	$0.″286 \pm 0.″146$	3.072 ± 2.476	$21.822^{+1.298}_{-0.575}$	1.903	$7.7\% \pm 2.4\%$	$23.671^{+0.403}_{-0.293}$	
CID216	1.514	$93.9\% \pm 4.7\%$	$0.″251 \pm 0.″063$	6.159 ± 1.205	$21.51^{+0.052}_{-0.049}$	1.425	$35.1\% \pm 1.5\%$	$23.446^{+0.053}_{-0.051}$	
CID237	2.349	$29.9\% \pm 6.3\%$	$0.″872 \pm 0.″172$	4.736 ± 1.701	$21.279^{+0.26}_{-0.209}$	2.354	$3.2\% \pm 2.0\%$	$23.718^{+1.037}_{-0.52}$	
CID255	...	...	...	...	...	...	...	...	
CID3242	2.751	$46.1\% \pm 12.7\%$	$0.″201 \pm 0.″159$	6.142 ± 1.874	$21.161^{+0.35}_{-0.264}$	2.596	$4.8\% \pm 1.3\%$	$23.595^{+0.337}_{-0.257}$	
CID3570	1.665	$76.5\% \pm 1.6\%$	$0.″698 \pm 0.″007$	0.728 ± 0.054	$21.164^{+0.021}_{-0.021}$	1.332	$85.6\% \pm 1.5\%$	$22.971^{+0.012}_{-0.012}$	
CID452	1.684	$75.4\% \pm 3.9\%$	$0.″365 \pm 0.″015$	1.402 ± 0.175	$21.176^{+0.063}_{-0.06}$	1.452	$37.8\% \pm 0.7\%$	$22.732^{+0.022}_{-0.022}$	
CID454	2.203	$35.8\% \pm 2.5\%$	$0.″388 \pm 0.″016$	0.624 ± 0.106	$21.196^{+0.08}_{-0.074}$	1.291	$9.2\% \pm 0.5\%$	$23.352^{+0.058}_{-0.055}$	
CID50	5.576	$16.5\% \pm 9.0\%$	$0.″163 \pm 0.″11$	3.217 ± 2.223	$20.934^{+0.863}_{-0.475}$	4.940	$5.0\% \pm 3.3\%$	$22.504^{+1.145}_{-0.545}$	
CID543	1.902	$30.6\% \pm 9.7\%$	$0.″1 \pm 0.″0$	0.493 ± 0.325	$21.994^{+0.406}_{-0.295}$	1.435	$5.2\% \pm 2.0\%$	$23.765^{+0.534}_{-0.357}$	
CID597	1.565	$42.4\% \pm 16.6\%$	$0.″173 \pm 0.″058$	1.752 ± 0.784	$21.868^{+0.543}_{-0.36}$	1.254	$11.5\% \pm 1.3\%$	$23.563^{+0.126}_{-0.113}$	
CID607	1.692	$43.6\% \pm 17.9\%$	$0.″206 \pm 0.″087$	3.418 ± 1.097	$21.189^{+0.575}_{-0.374}$	2.590	$4.7\% \pm 1.8\%$	$23.566^{+0.511}_{-0.346}$	
CID70	2.041	$19.7\% \pm 4.9\%$	$0.″422 \pm 0.″095$	3.616 ± 1.028	$21.862^{+0.304}_{-0.237}$	2.361	$2.3\% \pm 1.1\%$	$24.625^{+0.677}_{-0.414}$	
LID1273	1.697	$53.3\% \pm 9.1\%$	$0.″302 \pm 0.″04$	1.22 ± 0.49	$20.939^{+0.211}_{-0.176}$	2.137	$6.4\% \pm 0.8\%$	$23.289^{+0.153}_{-0.134}$	
LID1538	2.362	$43.5\% \pm 7.8\%$	$0.″177 \pm 0.″042$	2.819 ± 0.475	$21.251^{+0.221}_{-0.184}$	2.173	$7.5\% \pm 1.2\%$	$23.088^{+0.189}_{-0.161}$	
LID360	3.918	$18.4\% \pm 2.0\%$	$0.″626 \pm 0.″02$	0.752 ± 0.355	$21.455^{+0.136}_{-0.121}$	4.914	$3.7\% \pm 0.5\%$	$23.254^{+0.172}_{-0.149}$	
XID2138	1.597	$38.9\% \pm 5.5\%$	$0.″498 \pm 0.″033$	1.24 ± 0.391	$21.869^{+0.172}_{-0.148}$	2.731	$5.0\% \pm 1.3\%$	$23.898^{+0.313}_{-0.243}$	
XID2202	3.23	$33.3\% \pm 8.0\%$	$0.″1 \pm 0.″001$	3.957 ± 1.017	$21.16^{+0.302}_{-0.236}$	3.852	$8.3\% \pm 1.9\%$	$22.592^{+0.286}_{-0.226}$	
XID2396	3.669	$23.9\% \pm 10.5\%$	$0.″584 \pm 0.″085$	0.772 ± 1.36	$21.404^{+0.652}_{-0.404}$	5.346	$2.3\% \pm 0.5\%$	$23.364^{+0.243}_{-0.198}$	
CDFS-1	1.358	$64.5\% \pm 19.7\%$	$0.″137 \pm 0.″069$	4.806 ± 1.112	$22.468^{+0.397}_{-0.29}$	...	...	...	
CDFS-229	4.329	$17.6\% \pm 2.1\%$	$0.″507 \pm 0.″026$	0.463 ± 0.195	$21.568^{+0.144}_{-0.127}$	...	...	...	
CDFS-321	3.998	$24.5\% \pm 11.7\%$	$0.″378 \pm 0.″122$	2.26 ± 2.007	$20.337^{+0.703}_{-0.423}$	...	...	...	
CDFS-724	1.355	$34.7\% \pm 14.6\%$	$0.″118 \pm 0.″03$	1.618 ± 1.099	$23.695^{+0.582}_{-0.377}$	...	...	...	
ECDFS-358	2.012	$56.4\% \pm 13.5\%$	$0.″359 \pm 0.″043$	1.671 ± 0.542	$21.34^{+0.302}_{-0.236}$	...	...	...	
SXDS-X1136	1.937	$40.5\% \pm 7.8\%$	$0.″101 \pm 0.″003$	1.986 ± 0.483	$21.921^{+0.231}_{-0.19}$	...	...	...	
SXDS-X50	1.423	$40.7\% \pm 8.6\%$	$0.″192 \pm 0.″04$	1.648 ± 0.621	$21.988^{+0.267}_{-0.214}$	...	...	...	
SXDS-X717	1.426	$61.4\% \pm 9.1\%$	$0.″264 \pm 0.″066$	5.58 ± 1.421	$21.759^{+0.176}_{-0.151}$	...	...	...	
SXDS-X735	2.203	$32.4\% \pm 8.5\%$	$0.″22 \pm 0.″057$	2.027 ± 1.012	$20.919^{+0.333}_{-0.254}$	...	...	...	
SXDS-X763	2.376	$6.0\% \pm 4.0\%$	$0.″694 \pm 0.″532$	2.394 ± 0.796	$24.134^{+1.172}_{-0.55}$	...	...	...	
SXDS-X969	1.613	$29.1\% \pm 11.1\%$	$0.″11 \pm 0.″019$	2.053 ± 1.071	$21.591^{+0.515}_{-0.348}$	...	...	...	

NOTE. — Column 1: Object ID. Column 2: Reduced χ^2 value by the best PSF in the library. Column 3-6: WFC3 inference. Column 7-9: ACS inference. Column 10: Inferred host Luminosity in the rest-frame R band.

TABLE 4
INFERRED $\mathcal{M}_{\mathrm{BH}}$.

Target ID	using emission line $H\alpha$			using emission line $H\beta$		
	FWHM (km s^{-1})	log(λL$_{H\alpha}$) (erg s^{-1})	$\mathcal{M}_{\mathrm{BH}}$ (M$_\odot$)	FWHM(5100) (km s^{-1})	log(λL$_{\lambda 5100}$) (erg s^{-1})	$\mathcal{M}_{\mathrm{BH}}$ (M$_\odot$)
(1)	(2)	(3)	(4)	(5)	(6)	(7)
CID1174	1906.3037	43.43237	7.992	5898.264	44.76243	8.833
CID1281	1619.4891	43.23945	7.749	...	...	...
CID206	3333.5527	43.4776	8.528	...	...	...
CID216	2229.5232	42.84509	7.854	...	...	...
CID237	2112.3306	43.85546	8.289	...	...	...
CID255	1932.0933	43.9924	8.273	3709.241	45.37122	8.734
CID3242	2543.2202	43.83323	8.449	3774.503	45.09891	8.613
CID3570	1958.8551	43.16374	7.888	...	...	...
CID452	3457.8801	42.92298	8.295	3127.3306	44.63353	8.217
CID454	2824.2693	43.34466	8.311	...	...	...
CID50	2339.9104	43.93786	8.423	1938.5676	45.32766	8.149
CID543	2188.8447	43.57404	8.187	...	...	...
CID597	1656.3296	43.32955	7.813	...	...	...
CID607	3009.1816	43.67079	8.526	4241.526	44.78209	8.556
CID70	2480.4058	43.50531	8.269	3981.8574	45.1582	8.689
LID1273	3223.8484	43.61001	8.561	...	...	...
LID1538	2941.422	43.59594	8.469	...	...	...
LID360	2481.7253	43.88091	8.45	2868.8992	45.08676	8.369
XID2138	3185.8613	43.6148	8.552	2944.7766	44.80782	8.252
XID2202	2973.2378	43.56249	8.463	...	...	...
XID2396	2271.2617	44.06196	8.455	2657.8386	45.50467	8.511
CDFS-1	...	...	...	...	...	...
CDFS-229	...	...	...	...	...	...
CDFS-321	2441.93	43.92714	8.457	...	...	...
CDFS-724	...	...	...	...	...	...
ECDFS-358	2237.2314	43.39674	8.122	...	...	...
SXDS-X1136	2759.8953	43.43305	8.333	6761.222	44.71429	8.927
SXDS-X50	1816.672	43.421	7.942	...	...	...
SXDS-X717	2930.7417	43.04988	8.204	...	...	...
SXDS-X735	2702.0962	43.69804	8.44	3519.6052	45.07463	8.54
SXDS-X763	2961.1743	43.57321	8.465	4508.5146	44.51285	8.474
SXDS-X969	2296.0566	43.50066	8.196	1695.7146	45.05337	7.895

NOTE. — Column 1: Object ID. Column 2-4: $H\alpha$ emission line width (FWHM), continuum luminosity, and inferred $\mathcal{M}_{\mathrm{BH}}$. Column 5-7: $H\beta$ emission line width (FWHM), continuum luminosity, and inferred $\mathcal{M}_{\mathrm{BH}}$.
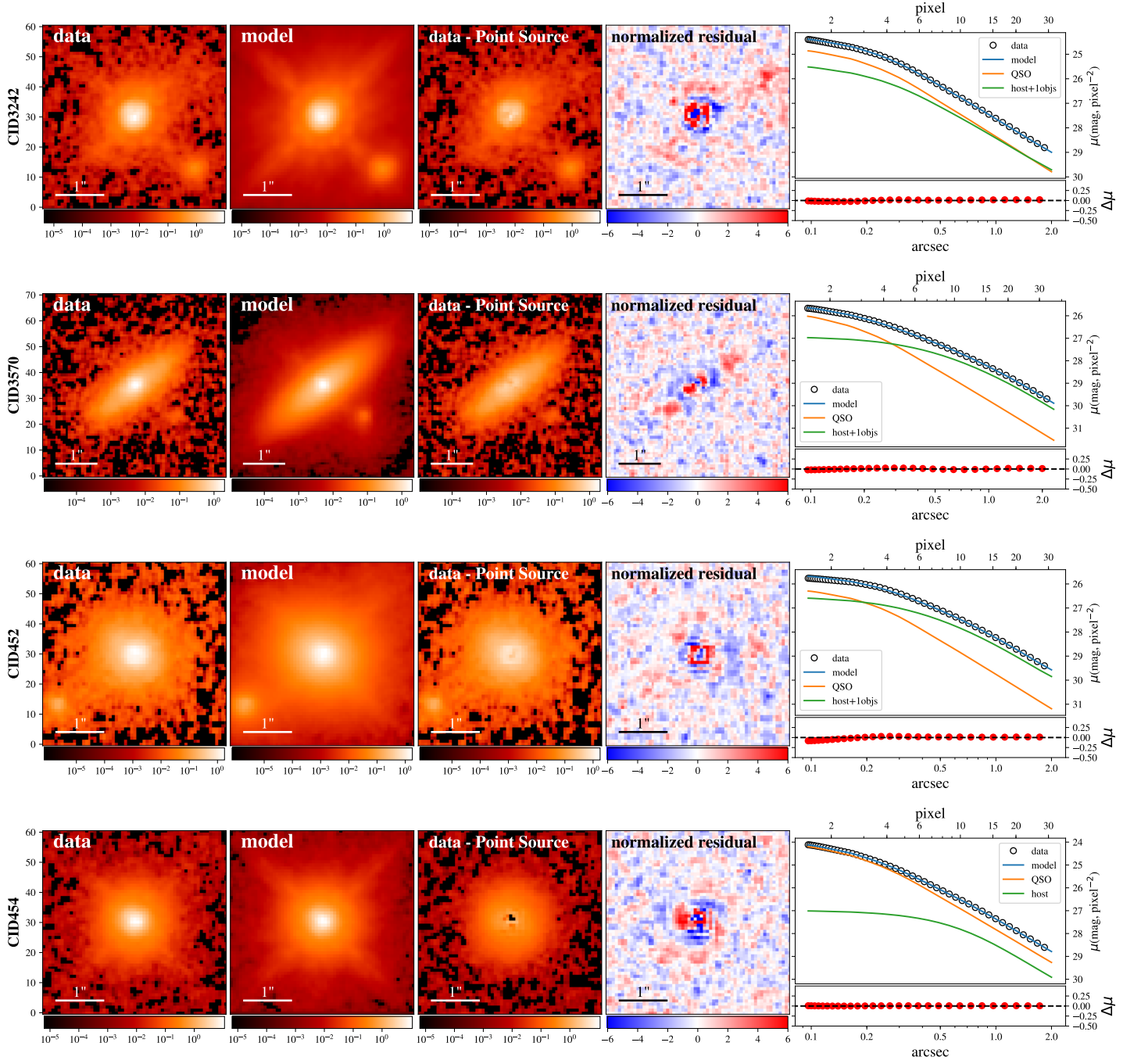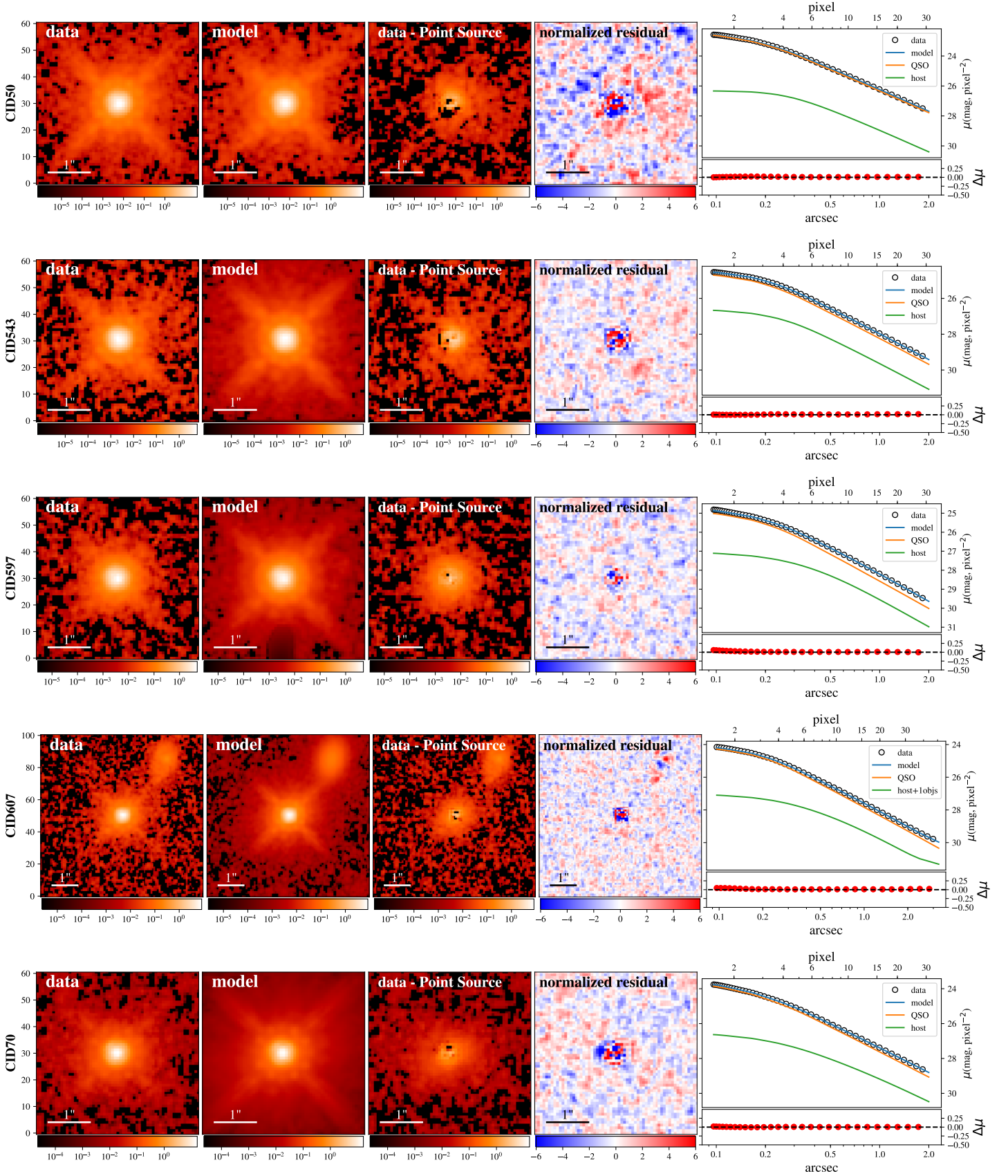
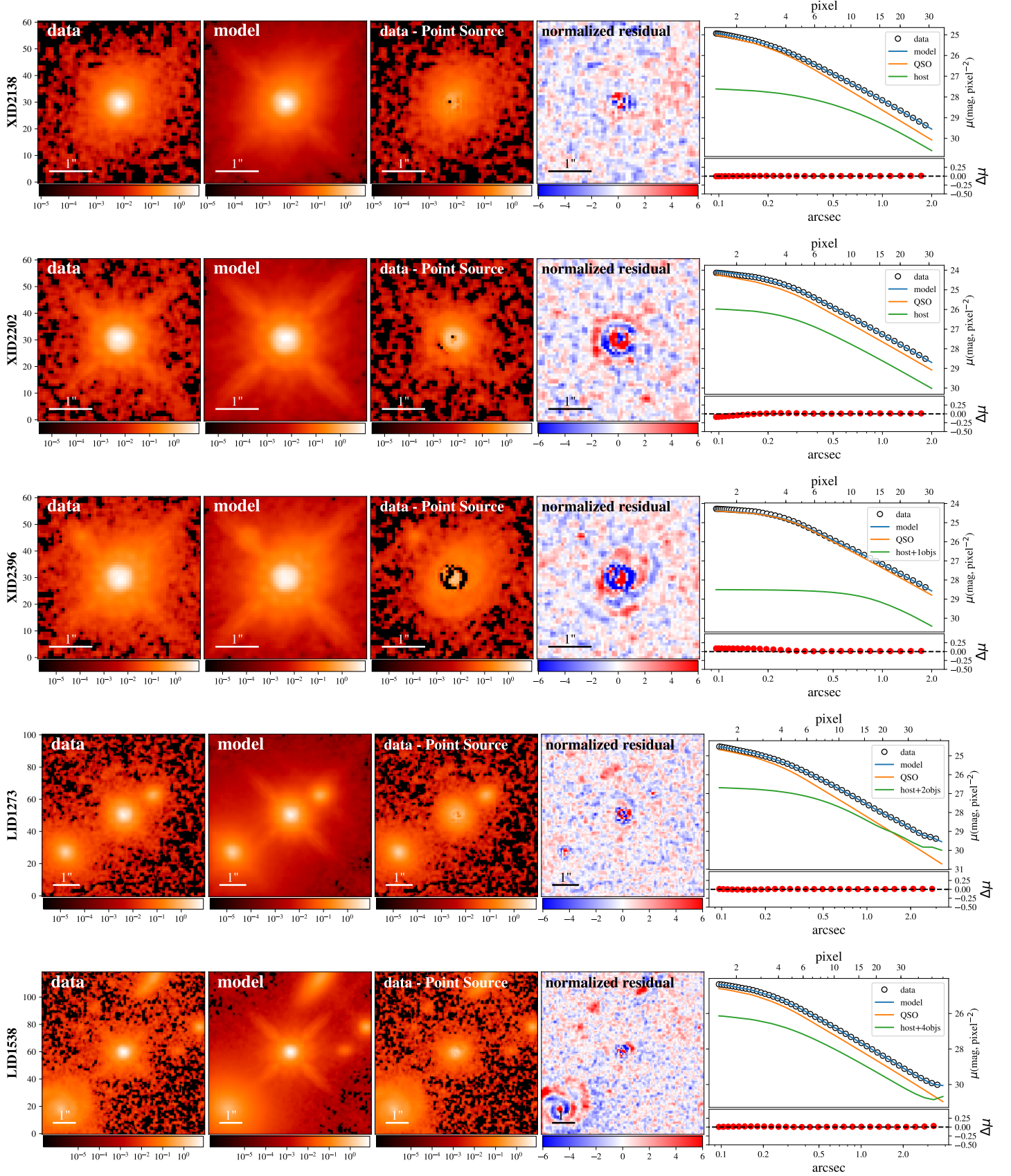FIG. 1.— Figure illustrates the inference for the 32 objects based on the WFC3 images. In each row, observed data (first column), best-fit models (second column), data subtracted by the inferred point source (third column), normalized residuals (fourth column) are presented together with the target ID. In the fifth column, we present the 1-D surface brightness profiles (top) and the corresponding residual (bottom). The 1-D profiles indicate the surface brightness including the data (open circles), the best-fit model (blue line), the AGN (orange line), and the model for the extended sources (green line, i.e., host and other objects). Note that the one-dimensional surface brightness profiles are only for illustration purposes. The actual fitting is based on the two-dimensional images.

FIG. 1.— Continued.
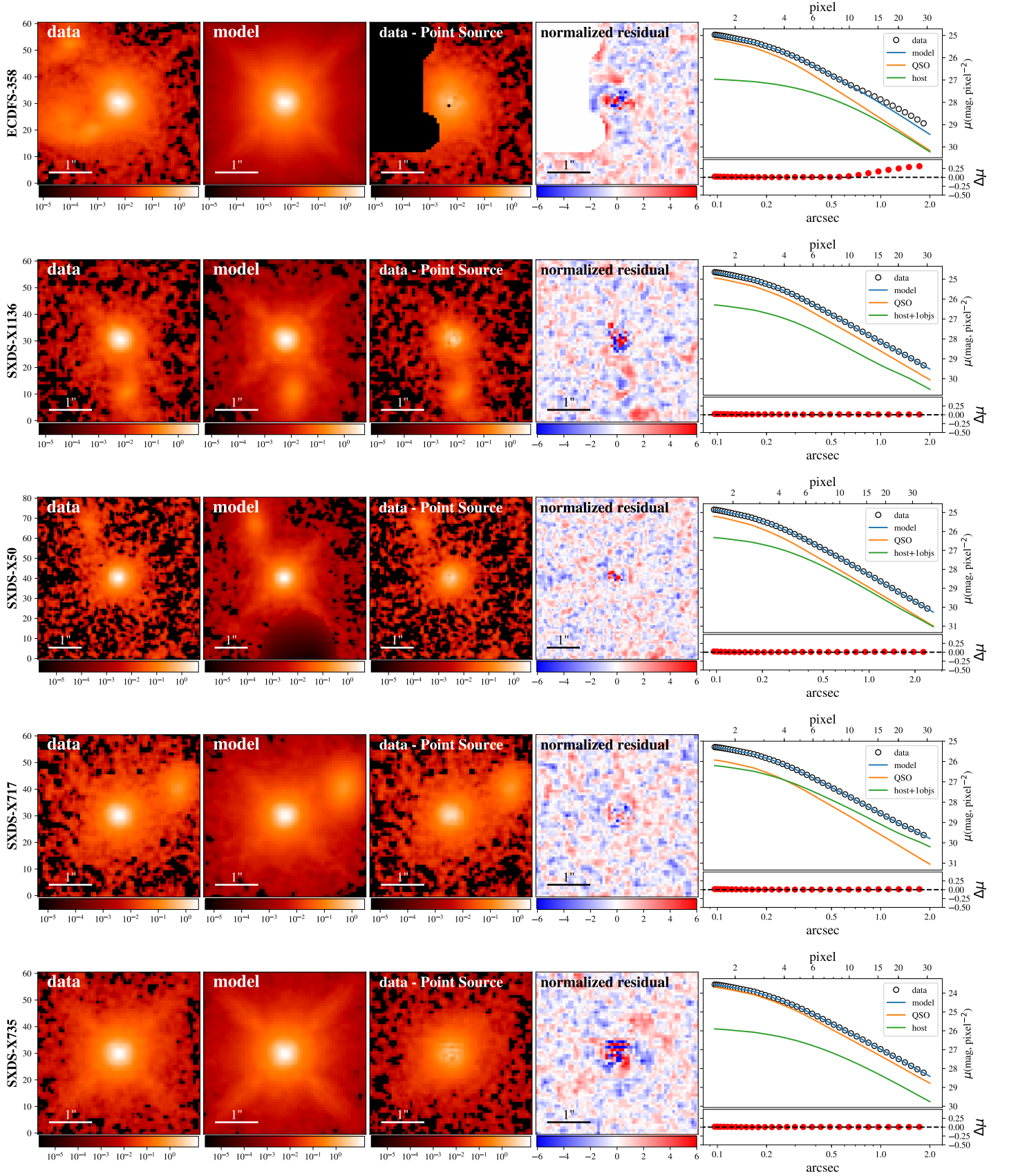
FIG. 1.— Continued.

FIG. 1.— Continued.

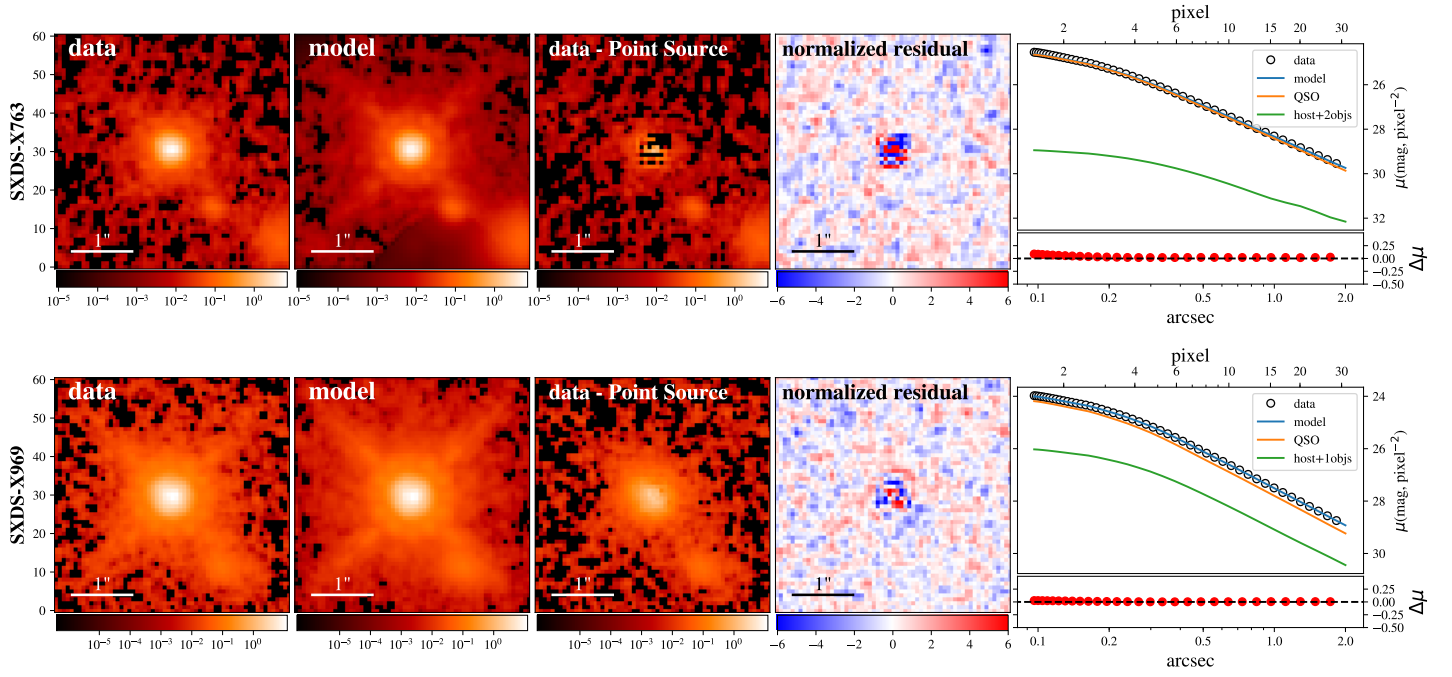Fig. 1.— Continued.

FIG. 1.— Continued.
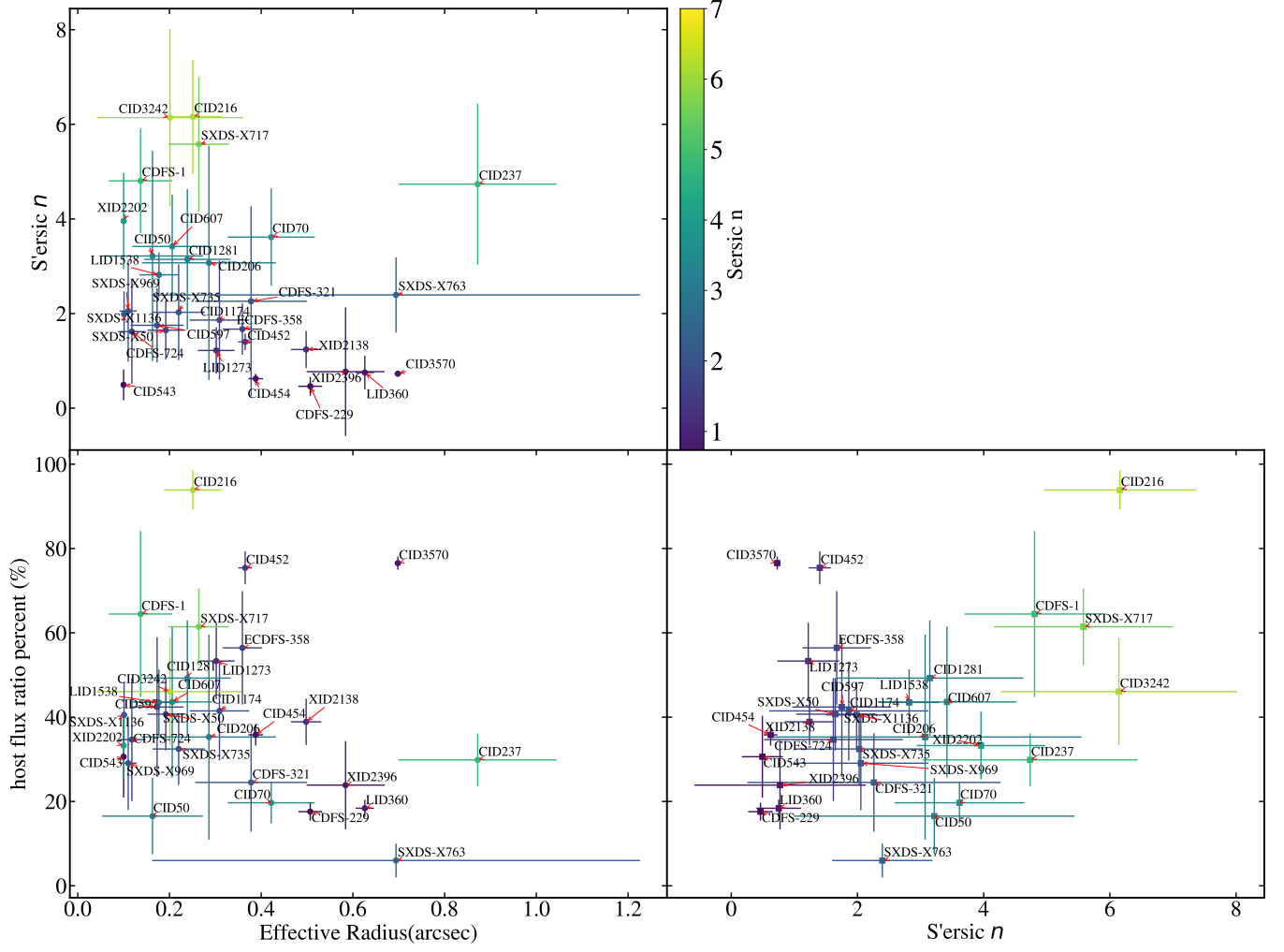
Fig. 1.— Continued.

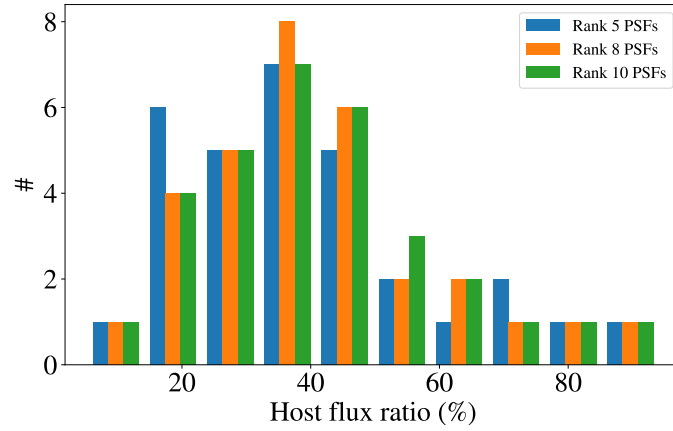FIG. 2.— Illustration of the relations between the inferred host properties.

FIG. 3.— Comparison of the histogram of the inferred host flux ratio, based on the different amount of the top-ranked PSFs.